Cold Regions Science and Technology 241 (2026) 104699

Contents lists available at ScienceDirect

Cold Regions Science and Technology

journal homepage: www.elsevier.com/locate/coldregions

Microstructural insight into the effect of fine content on frost heave in clayey sand mixtures

Giulia Guida [a,b,*], Floriana Anselmucci [b], Francesca Casini [a], Vanessa Magnanimo [b]

[a] Dipartimento di Ing. Civile e Ing. Informatica, Università degli Studi di Roma Tor Vergata, via del Politecnico 1, Rome, 00133, Italy
[b] Soil Micro Mechanics, Department of Civil Engineering and Management, Faculty of Engineering Technology, University of Twente, Drienerlolaan 5, Enschede, 7522NB, The Netherlands

ARTICLE INFO

Keywords:
Frost-heave
In situ X-ray CT
Freeze-thaw cycles
THM processes

ABSTRACT

This study investigates the complex thermo-hydro-mechanical response of frost-susceptible soils subjected to freezing and thawing, using *in situ* X-ray computed tomography. Five saturated clayey sand mixtures with varying kaolin contents have been subjected to two freeze-thaw cycles by means of a cooling plate. X-ray computed tomography enabled the reconstruction of three-dimensional images of the samples at different deformation stages during the thermal process, revealing the influence of fine content on the microstructure evolution. The soil response to freeze-thaw cycles is shown to be highly heterogeneous, with local axial deformation exceeding 100%, especially in the central regions of samples with higher fine content. During freezing, frost heave ratios reached 25%, 47%, 66%, for mixtures with 5%, 10% and 20% of kaolin, respectively, and up to 78% for the mixture with 50% kaolin, the main cause of deformation being the water migration driven by fine pores. Upon thawing, the soil rarely returns to its initial undeformed state, often resulting in a significantly altered microstructure. Image analysis provided both qualitative and quantitative insights into the evolving non-homogeneous density patterns and the localized phenomena occurring throughout the transient process.

1. Introduction

The behaviour of soils under sub-zero temperatures has significant implications for geotechnical and civil engineering applications, particularly in cold climates. When subjected to prolonged freezing temperatures, pore water within the soil transitions into ice, often leading to frost heave; *i.e.*, the upward movement of the soil surface caused by the volumetric expansion of soil upon freezing (Peppin and Style, 2013). Uplifts induced by freezing, as well as severe settlements of ice-rich soils during thawing, can result in structural damage of (infra)structures such as road pavements, foundations, embankments and high-speed railway subgrades (Taber, 1929; Hjort et al., 2022), especially when these ground movements are non-uniform.

Soil expansion due to freezing is influenced by a combination of factors, including environmental temperatures, soil type, density state, water content, stress state, salinity (Cui et al., 2024) and the presence of aquifers or a phreatic water table (Taber, 1929; Chamberlain, 1982). Frost heave cannot be attributed solely to the change in volume of the water contained in the soil, given that ice (917 kg/m^3) has a lower density than liquid water (999 kg/m^3). Excessive heaving is always due to migration of additional water driven by a pressure gradient towards colder zones of the subsurface and ice lens formation with the consequent segregation. The effects of water redistribution, ice lenses and overall volume change of the soil drive the evolution of the material's microstructure, leading to a local increase in macropores, *e.g.*, An et al. (2021) and Fan et al. (2021). Upon thawing, the material often fails to recover its initial microstructure, resulting in significant and irreversible rearrangements (Chamberlain and Gow, 1979; Hohmann-Porebska, 2002), leading, in turn, to shear strength (Konrad and Morgenstern, 1980) and permeability (Dalla Santa et al., 2019) degradation.

The fully three-dimensional and spacially heterogeneous nature of the microstructural changes induced by freeze-thaw processes requires continuous data acquisition over the entire surface or volume of the specimen to be properly captured (*i.e.*, full-field measurements Viggiani et al., 2015). Conventional observation techniques, such as 2D imaging, struggle to capture the complexity of these changes, particularly their three dimensional characteristics. For example, Arenson et al. (2007) studied the formation and growth of ice lenses by means of time-laps photography, while Akagawa (1988) combined a conventional open-system frost heave test with two-dimensional X-ray radiography

---

* Corresponding author at: Dipartimento di Ing. Civile e Ing. Informatica, Università degli Studi di Roma Tor Vergata, via del Politecnico 1, Rome, 00133, Italy.

E-mail addresses: giulia.guida@uniroma2.it, g.guida@utwente.nl (G. Guida).

https://doi.org/10.1016/j.coldregions.2025.104699
Received 9 June 2025; Received in revised form 6 September 2025; Accepted 23 September 2025

to investigate frozen fringe. However, both approaches failed to capture the three-dimensional full-field nature of the ice pattern. Nuclear Magnetic Resonance (NMR) can serve as a full-field, non-destructive test, *e.g.*, to map local unfrozen water content during freezing-thawing cycles (Tian et al., 2018). Neutron tomography is another powerful non-destructively method for studying frost heave due to its sensibility to light elements such as hydrogen; differences in the neutron attenuation coefficients between crystalline ice and liquid water allow ice melting process to be explored with relative ease (Kalvoda et al., 2019). However, its accessibility is limited. The mechanics of frozen soils, though complex, can be effectively investigated using X-ray Computed Tomography (CT). Volume tracking of phase change materials during both melting and solidification can be successfully performed thanks to the density difference between ice and liquid water (Martinez-Garcia et al., 2023), though proper pore scale investigations require high spatial resolution. Calmels and Allard (2008) subjected permafrost cores to X-ray radiography to extract a three-dimensional perspective of the cryostructures along the depth; Fan et al. (2021) explored the impact of freeze-thaw cycles on macropores and fissure redistribution in clay. X-rays CT is particularly well-suited for detecting the three-dimensional pattern of ice-lenses within a fine matrix, *e.g.*, silty loam (Torrance et al., 2008). Furthermore, *in situ* X-ray CT scanning enables tracking the freezing process when a compact experimental apparatus is mounted on the CT stage. For example, Nakamura et al. (2021) scanned samples of natural soils with varying degrees of frost-susceptibility during deformation. Similarly, Amato et al. (2022) investigated the effect of thermal gradient on closed system (*i.e.*, no water entry) remoulded clay samples and observed that even when the freezing advances in one dimension, the resulting ice lenses exhibit a complex three-dimensional structure that strongly affects the local density within the specimen (Viggiani et al., 2015).

Despite advancements in the field and emerging technologies, the microstructural changes occurring in soils during freeze-thaw cycles remain poorly understood and the development of a reliable tool to predict the behaviour of frost-susceptible soils is still missing. This study is among the first to present a comparative analysis of the responses of clayey sand binary mixtures subjected to freeze-thaw cycles, using *in situ* X-ray CT and image processing. The role of fines was isolated to enable a systematic investigation of the effect on key quantities, namely frost heave, internal deformation and density heterogeneity. While previous studies have applied in situ CT to natural or remoulded fine-grained soils, this study exploits CT scanning to investigate *ad hoc* designed artificial mixtures and provides a quantitative assessment of how clay contents influences the material microstructure during freezing-thawing cycles. The findings address gaps in current knowledge and advance our understanding of volumetric soil behaviour at sub-zero temperatures.

The paper begins by introducing the basic concepts of frost susceptibility – a key factor that motivated the use of sandy mixtures with varying clay content. Then, it describes in detail the experimental campaign, including materials used, sample preparation and the *in situ* X-ray tomography freeze-thaw test setup. The resulting three-dimensional images are interpreted both quantitatively and qualitatively to investigate the hydro-mechanical responses, as well as the heterogeneous density patterns of the material microstructure as a function of the fine content.

2. Frost susceptibility

Frost susceptibility refers to the capacity of the soil to generate frost heave, which results from the interplay of environmental conditions and soil properties (Haosong et al., 2024). While some authors proposed to relate frost susceptibility directly to specific laboratory test results (Konrad, 1999; Zhou et al., 2022), it is well known that the grain size distribution is a crucial ingredient for the frost susceptibility. Graded mixtures of fine sand and silt or clay are particularly prone to frost heave, due to high water retention capacity and susceptibility to capillarity. Casagrande (1931) proposed a method to classify frost susceptibility by the percentage of fine content, while empirical classification systems, which indirectly relate soil properties – such as grain size distribution, soil plasticity and hydraulic conductivity – to frost susceptibility, are still widely used in engineering practice (Armstrong and Csathy, 1963; Chamberlain, 1982).

2.1. Capillary theory applied to frozen soils

In unfrozen soils, capillary forces govern water retention and movement within the pore spaces. These forces arise due to surface tension at the air–water interface and the interaction between water molecules and soil particles. Smaller pore sizes lead to higher capillary rise, explaining why fine-grained soils (*e.g.*, silts, clays) retain more water than coarse-grained soils (*e.g.*, sands, gravels). This approach can be extended to frozen soils to explain how water migrates through the soil matrix and contributes to frost heave (Konrad and Morgenstern, 1980). When the soil temperature drops below 0 °C, not all water freezes immediately, a portion remains in a liquid state. When ice and liquid water co-exist in a pore, the interface tension generated at the freezing front – due to the pressure difference between the two water phases, otherwise called cryogenic suction – is the higher the smaller is the curvature radius r of the interface between ice and liquid water adjacent to a pore, assumed to approximate a spherical cap. Following the Young–Laplace Equation, the pressure difference is:

$$P_i - P_w = \frac{2\gamma_{iw}}{r}, \tag{1}$$

where γ_{iw} is the ice–water surface tension equal to 0.0756 Nm^{-1} at 0 °C, P_i and P_w are the ice and liquid water pressures. Assuming a proportionality between pore size and grain size, particularly true in uniformly graded soils (Mitchell et al., 2005), Eq. (1) explains why high cryogenic suction levels develop with fine content.

Additionally, Clausius-Clapeyron Equation (2) can be used to describe the thermodynamic equilibrium of a system containing ice and liquid water at pressures P_i and P_w, respectively (Nishimura et al., 2009), explaining why the pressure difference locally diminished when the temperature T decreases, inducing a pressure gradient, *i.e.*, water migration, towards the colder temperatures.

$$P_i - P_w = \left(\frac{\rho_i}{\rho_w} - 1\right) P_w - \frac{\rho_i L_f}{T_m}(T_m - T). \tag{2}$$

Here ρ_w and ρ_i are the density of water and ice, respectively and L_f is the latent heat of fusion at the bulk temperature T_m.

3. Experimental campaign

3.1. Materials

Four different artificially constituted binary mixtures are considered, composed of saturated Fontainebleau sand with 5%, 10%, 20% and 50% dry mass fractions of Speswhite kaolin, following the approach adopted in Viglianti et al. (2024) and Vu et al. (2022). Such engineered sand-clay mixtures are commonly used in laboratory experiments as they offer good repeatability of results, exhibit mechanical behaviour typical of transitional soils and are more readily available than natural soils (Purwana and Nikraz, 2015). Fontainebleau sand is characterized by a uniform grain size distribution, with a median particle diameter of $D_{50} = 210$ μm and coefficient of uniformity $C_u = D_{60}/D_{10} = 1.52$ (measure of gradation). In contrast, Speswhite kaolin consists of fine particles, 80% of which have diameters smaller than 2 μm, and is characterized by a high specific surface area of approximately 30 m^2/g. The specific gravity is $G_s = 2.65$ for both constituent materials. Refer to Vu et al. (2022) for additional information on the physical properties of the two constituent materials (Fontainbleau sand and Speswhite kaolin), both individually and in

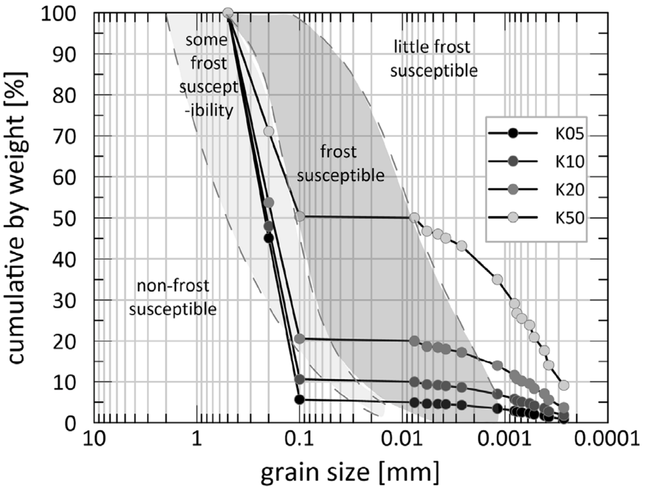

Fig. 1. Grain size distribution of the clayey sand mixtures used in this study, superimposed to the frost-susceptibility map after (Armstrong and Csathy, 1963).

artificial mixtures with different proportions. Fig. 1 reports the grain size distribution of the mixtures adopted in this study superimposed to a map of frost susceptibility as proposed by Armstrong and Csathy (1963). Increasing the percentage by weight of fine content, from 5% to 50%, gives the material an enhanced degree of frost-susceptibility.

Fig. 2 shows optical microscope *versus* X-ray tomography images of the four mixtures. Optical images use visible light to show the mixture surface and only sand grains immersed in the clay matrix are distinguishable in the left panels of Fig. 2. X-rays are a form of electromagnetic radiation with much shorter wavelengths than visible light, which can penetrate various objects depending on their density. Dense materials, such as soil solid particles block more X-rays, creating high contrast with less dense materials, such as liquids or gasses. In the X-ray images in the right panels of Fig. 2, the sand grains result clearer than the clay matrix, which contrasts sharply with the macropores, in black. Lower kaolin percentage samples are characterized by larger and isolated macro-pores, while samples with higher fine content show more uniformly distributed and smaller pore sizes.

According to the classification proposed by Park and Santamarina (2017), coarse-fine mixtures can be grouped based on the fine content: coarse-dominant (*e.g.*, kaolin 5% mix), where the main contact force network is sustained by the coarser grains; transitional (*e.g.*, kaolin 5% and 10% mixes), where both fines and coarse particles play a relevant role; and fines-dominant (*e.g.*, kaolin 50% mix), where coarse grains are no longer in contact and the internal structure of the mixture is primarily governed by the fine particles. As the kaolin percentage increases, the sand particles of Fig. 2 appear to lose contact and float in the clay matrix.

3.2. Samples preparation

The samples are prepared by pluviating the dry mixtures into Perspex cylinders with an internal diameter of 30 mm, without any compaction, in order to obtain initially loose configurations (see Fig. 3.a). The containers are then placed inside a vacuum bell, immersed in previously de-aerated tap water, and left to saturate from the bottom through their permeable base (Fig. 3.b). After 24 h of saturation, the samples are sealed at the base with a thermally conductive tape and a 10 mm water film is left at the top as a liquid water reservoir. In order to facilitate the traceability of the local kinematics, five glass beads with a diameter of 1.6 mm were buried into the sample at different depths. A summary of the initial state of the four samples tested is reported in Table 1. The “dry” state corresponds to the state before saturation: W_s is the weight of the solid, h_0^{dry} is the height of the sample, e_0^{dry} is the void ratio, computed assuming the sample as a cylinder of diameter 30 mm and height equal to h_0^{dry}. The “wet state” refers to after saturation: W_w is the weight of water added to the sample, h_0^{wet} is the height of the wet sample, e_0^{wet} is the corresponding void ratio, w is the water content, defined as the ratio between the weight of the water and the weight of the solids and S_r is the degree of saturation defined as the volume of water over the volume of voids. The heights of the sample, both in dry and wet conditions, are measured at the centre of the sample to avoid possible curvatures due to the boundaries. A taller sample, consisting of a 10% clay mixture, is prepared following the same procedure as the others but with an initial dry height of 50 mm. This sample has been tested in only one freeze-thaw cycle for longer.

Fig. 3(c) shows the void ratio measurements of the clayey sand mixtures in both dry (before saturation) and wet (after saturation) states. Data include samples from this experimental campaign as well as others (unpublished) conducted on the same material using the same containers and procedures. The figure shows a systematic increase in the void ratio with kaolin content, with the effect being more pronounced in dry conditions. The void ratio ranges from $e_0^{dry} = 0.6$ for the 5% kaolin mixture to $e_0^{dry} = 4.0$ for the 70% kaolin mixture. Those values fall within the envelope defined by experimental measurements of the maximum and minimum dry void ratios.

The increasing trend clearly demonstrates that kaolin particles, even in small percentages, do not simply settle in the gaps between larger sand grains, as commonly observed in binary mixtures with fine content up to 30%–40% (Othman and Marto, 2018). Instead, they wrap around the sand grains, restricting their rearrangement. The wrapping effect can be attributed to the highly irregular shape of kaolin particles, which are extremely flat and elongated. This morphology hinders efficient packing, resulting in a very loose and highly unstable particle structure, particularly in dry conditions (Thevanayagam et al., 2000; Cubrinovski and Ishihara, 2002). Upon saturation, the void ratio of the sample reduces, with the magnitude of densification increasing with fine content. This suggests that water induces the collapse of the unstable structure, facilitating particle rearrangement and densification. The different behaviour upon saturation reflects the classification categories assigned to the mixes in Park and Santamarina (2017): the coarse-dominant K05 mixture slightly swells; the transitional mixtures (K10–K20) do not experience significant change in volume or show slightly densification; all the fine-dominant K50 mixes show a significant reduction in void ratio. Additionally, while the preparation of dry samples is hardly repeatable – as indicated by the wide scatter of the cross symbols of Fig. 3 – the collapsed structure appears to be quite consistent.

4. X-ray CT tests

4.1. Setup

The tests have been conducted at Delft University of Technology using the X-ray tomography apparatus (TESCAN CoreTOM), which allows real-time scanning of the sample throughout the experiments. Fig. 4 illustrates the X-ray tomography setup. Freeze-thaw cycles are replicated with the aid of a refrigeration system, consisting of a thermoelectric-Peltier cold plate cooler & heater (CP-061HT, TE-Technology), controlled by a bi-polar proportional–integral–derivative (PID) temperature controller (TC-36-25-RS232-UL, TE-Technology), capable of modulating power input from 12 V up to 36 V. The system is powered by a PS-24–6.5 A power supply (TE-Technology). The setup is mounted on a rotation stage, allowing the sample to assume different orientations during scans while remaining in contact with the cooling plate. Cylindrical samples are wrapped laterally with an insulation coat to minimize thermal dispersion, while the top remains exposed to room temperature (approximately 24 °C), ensuring a one-dimensional heat transfer condition.

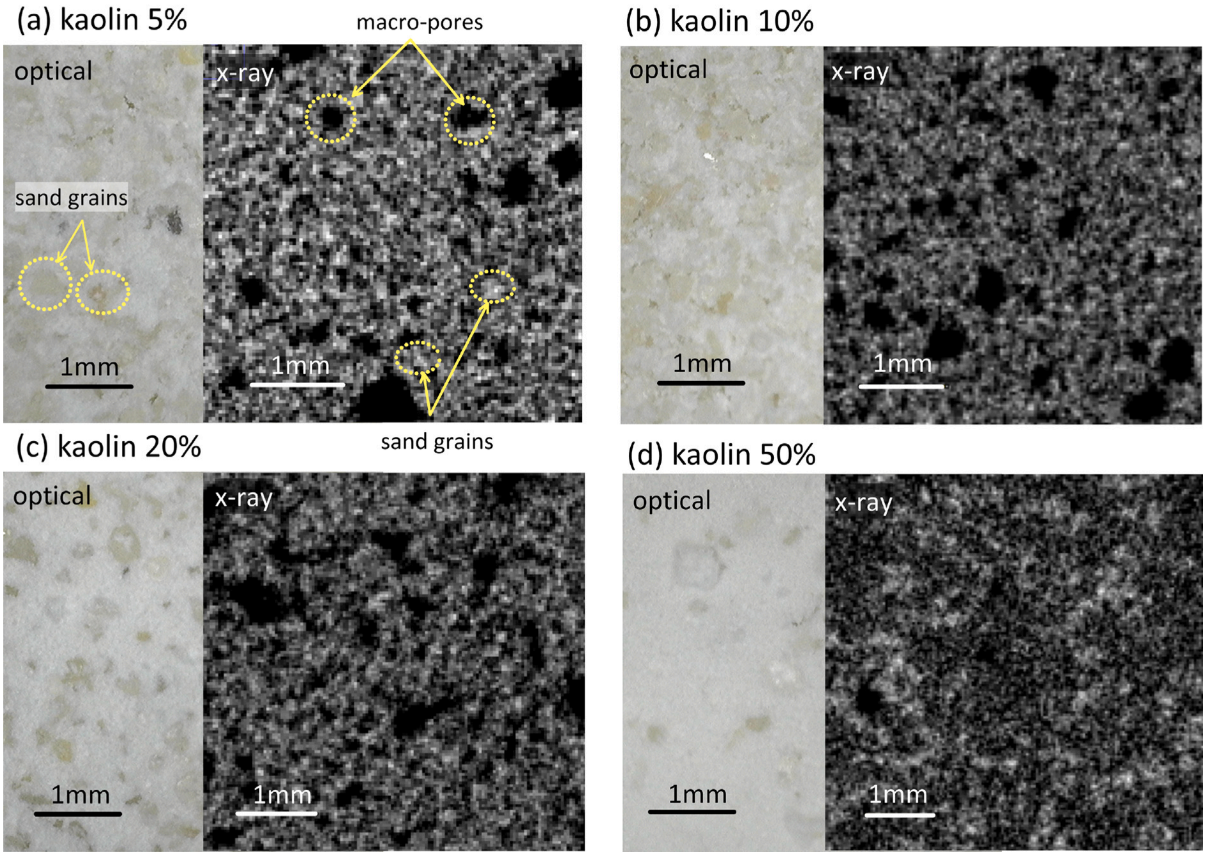

Fig. 2. Optical microscope images (magnification 40×) *versus* X-ray radiographs (resolution 36.6 μm/px) of the mixtures at different kaolin content: (a) 5%, (b) 10%, (c) 20% and (d) 50%.

Table 1
Samples dry and wet initial properties.

Sample	% clay	Dry state			Wet state				
		W_s [g]	h_0^{dry} [mm]	e_0^{dry} [–]	W_w [g]	h_0^{wet} [mm]	e_0^{wet} [–]	w [–]	S_r [–]
K05	5	31.9	27	0.58	7.48	29	0.70	0.23	0.88
K10	10	29.6	28	0.74	7.55	28	0.77	0.26	0.88
K20	20	23.4	27	1.12	7.68	25	1.00	0.33	0.87
K50	50	14.0	32	3.20	9.85	22	1.94	0.70	0.96
K10_2	10	55.2	49	0.65	10.87	48	0.63	0.20	0.83

At the top left of Fig. 4, the X-ray source, set at 140 kV with 1 mm Cu filter, emits a cone beam towards the detector screen, which measures the intensity of incident X-ray photons with an array of 2856 × 2856 pixels. X-ray tomography reconstructs a three-dimensional (3D) field of X-ray attenuation by acquiring multiple two-dimensional radiographs from different angles as the object rotates between X-ray source and detector. These images are then processed using specialized algorithms (Defrise, 2001) to generate a detailed 3D reconstruction of the sample's internal structure.

4.2. Freeze-thaw cycles

Four out of the five tests performed include two complete freeze-thaw cycles, consisting of 2 h freezing followed by 1 h thawing, for a total test duration of approximately 6 h. Fig. 5(a) presents the evolution of the cooling plate temperature throughout the freeze-thaw tests of samples K05–K50. The initial state corresponds to thermal equilibrium of the sample at the ambient temperature. The freezing process initiates by setting the cooling plate to the temperature of −15 °C, with the target temperature reached within approximately 10 min. During thawing, the cooling plate is switched off and its temperature rapidly matches the ambient temperature of 24 °C. The high ambient temperature significantly accelerated the thawing process, making 1 h sufficient for complete thawing of the sample. Throughout the two freeze-thaw cycles, the sample steady states are recorded at the key stages: initial, fully frozen and fully thawed. These states are captured using slow, 10-min scans at higher resolution (37.06 μm/px). In contrast, during the active deformation phases of freezing and thawing, faster 2-min scans at lower resolution (74.12 μm/px) are used to minimize image blurring caused by the high deformation rate. During freezing, two fast scans are taken every 40 min, while during thawing, a single fast scan is performed 30 min after the cooling plate is switched off.

Fig. 5(b) summarizes the X-ray scans performed during the extended freeze-thaw cycle on the tall sample K10_2. After the first scan, the following ones are taken every 10 min during the freezing phase, with the interval progressively increasing to 1 h for the final scan. During thawing, scans are again acquired every 10 min, except for the last one, which was taken after 20 min. All scans are short 2-min acquisitions at lower resolution (74.12 μm/px), except for the initial, fully frozen and thawed states, which are acquired using longer, higher resolution scans (37.06 μm/px).

The three-dimensional images are reconstructed from 2160 projections, using an exposure time of 250 ms for slow scans and 60 ms for

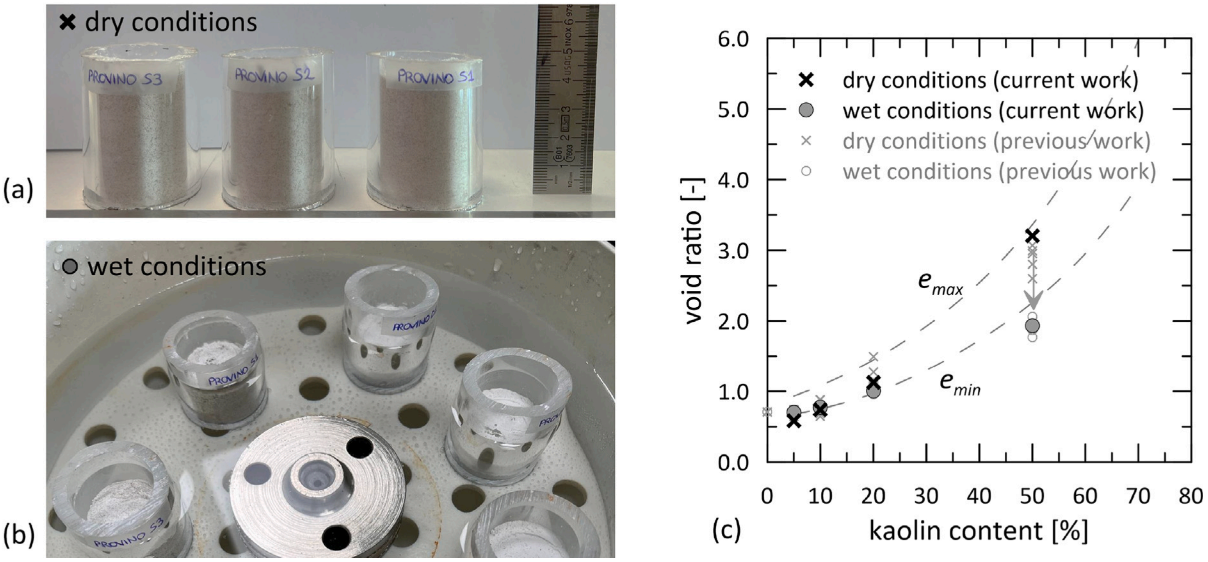

Fig. 3. (a) Image of dry mixtures, specifically three sample of K20, pluviated into the Perspex cylindrical containers; (b) Image of the samples immersed in tap water during saturation; (c) Void ratio measurements in dry and saturated conditions at different kaolin content.

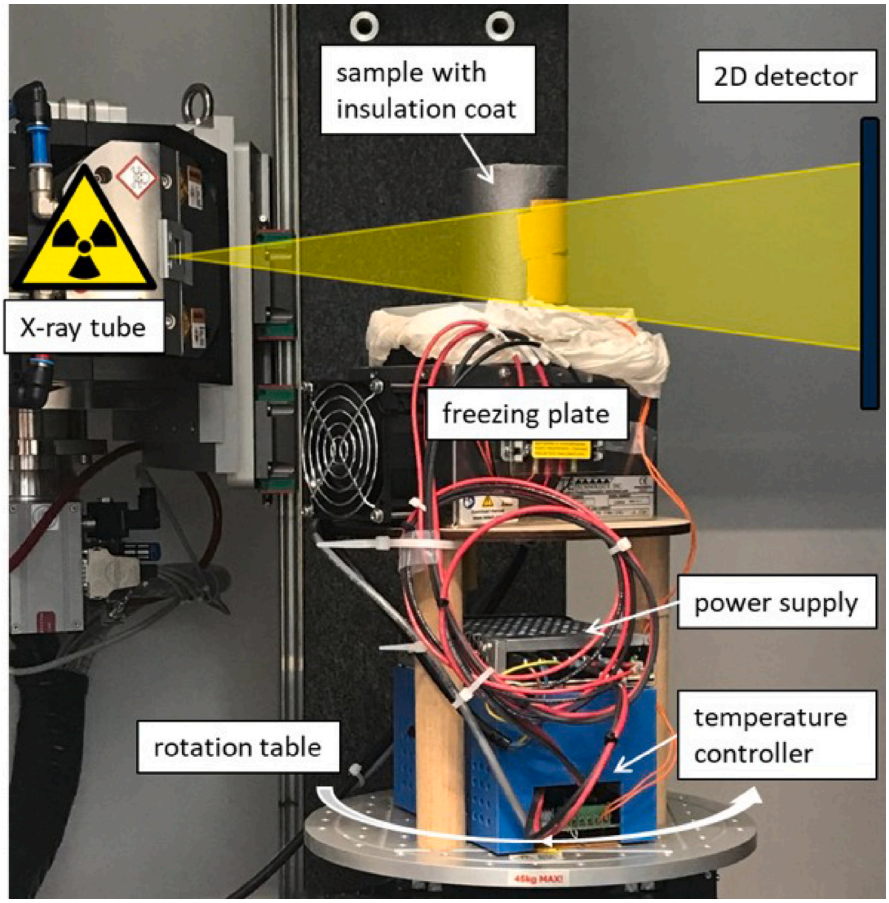

Fig. 4. X-ray tomography setup within the TESCAN-CoreTOM at TU Delft to perform *in situ* freeze-thaw tests.

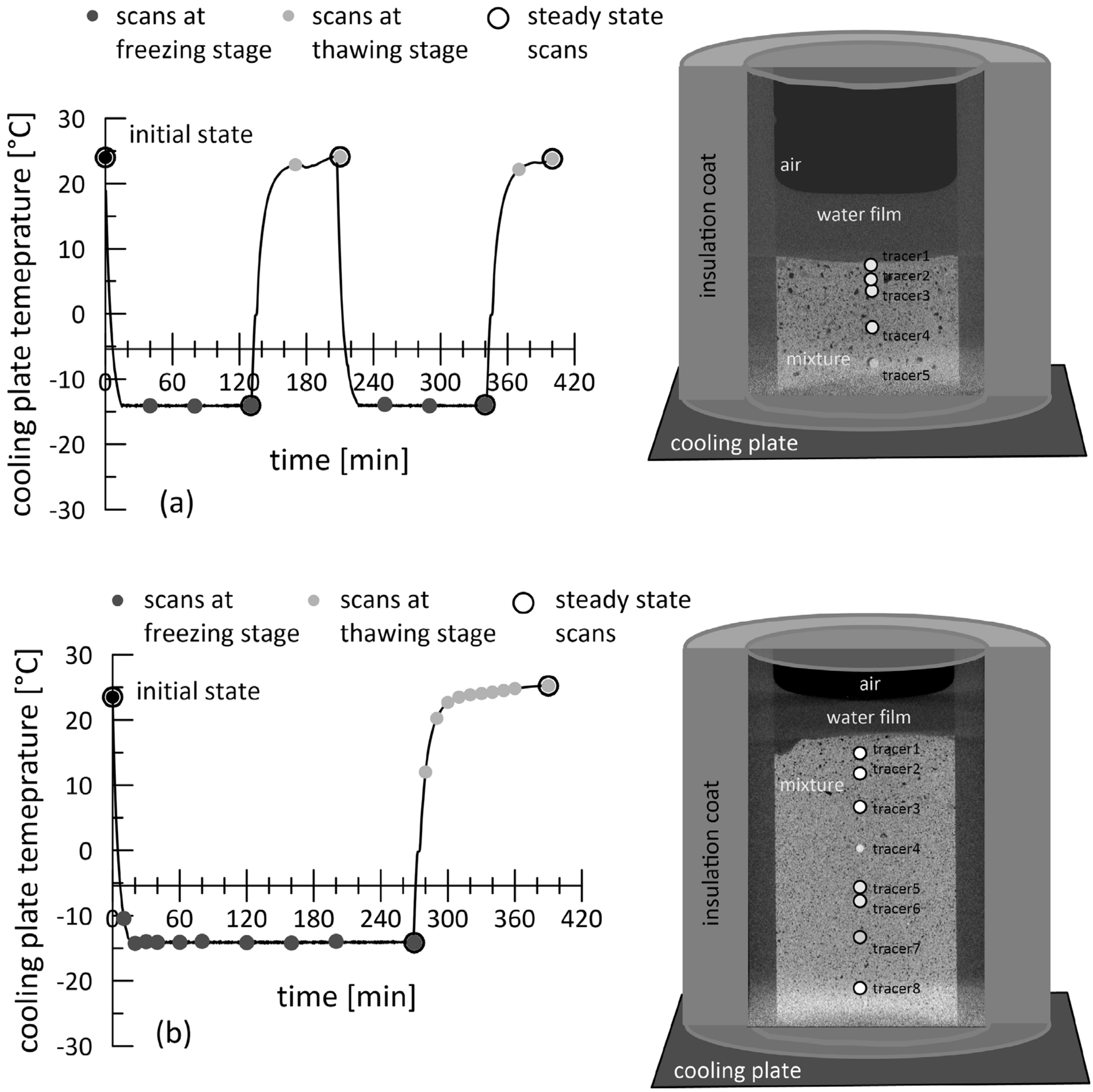

Fig. 5. Time evolution of the cooling plate temperature along (a) the two freeze-thaw cycles for samples K05–K50 and (b) the single freeze-thaw cycle for sample K10_2. On the right, vertical slice of the 3D reconstruction of the (a) K05 and (b) K10_2 samples at their initial stage, with a schematic view of the tracer positions.

fast scans. To ensure consistency across time, the grey-scale histograms of the images at various deformation stages are matched to the initial reference image of each test. This step ensures that the pixel intensity corresponding to a given material remains stable across scans, even under varying ambient conditions or global illumination level.

Fig. 5 also shows vertical slice images of the K05 and K10_2 samples in their initial state, reconstructed from the 3D scans. The material attenuating X-rays the most is that of the glass bead tracers. One of the tracers appears as a bright dot in both slices, while the remaining ones are only sketched to indicate their vertical position.

The white halo visible at the bottom of the sample is caused by the rectangular metal cooling plate, which does not match the circular geometry of the sample. This mismatch introduces image noise due to the conical shape of the X-ray beam and the high X-ray attenuation of metal. This issue could be partially mitigated by placing a cylindrical conductive stand (*e.g.*, made by copper) between the cooling plate and the sample, with a diameter matching that of the sample.

The vertical slice images shown in Fig. 6, obtained as two-dimensional sections of the 3D X-ray CT reconstructions at different time intervals, illustrate the evolution of the mixture containing 20% kaolin throughout the freeze-thaw test. Similar visualizations for the other tests are provided in the supplementary materials. The initial state is displayed at the top left, while the arrows guide the reader through the sequence of scans taken during freeze-thaw cycles. Freezing begins by setting and maintaining the cooling plate temperature at −15 °C for 120 min, during which the sample completely freezes. During this phase, the initially 12.6 mm thick film of liquid water at the top is gradually absorbed by the expanding soil mixture, leading to a height increase of 14.6 mm. The greyscale attenuation in the images reveals a denser (lighter in colour) top portion of the sample, which helps identify the position of the ice front.

Thawing begins at $t = 130$ min, once the cooling plate is switched off and its temperature gradually returns to ambient conditions. As the sides are insulated, melting starts from the top and bottom surfaces of the samples, which are exposed to room temperature. Due to gravity, the lower portion consolidates, separating from the still frozen central portion of the sample, whereas the upper unsaturated part remains unstably suspended along the container walls, segregated from the

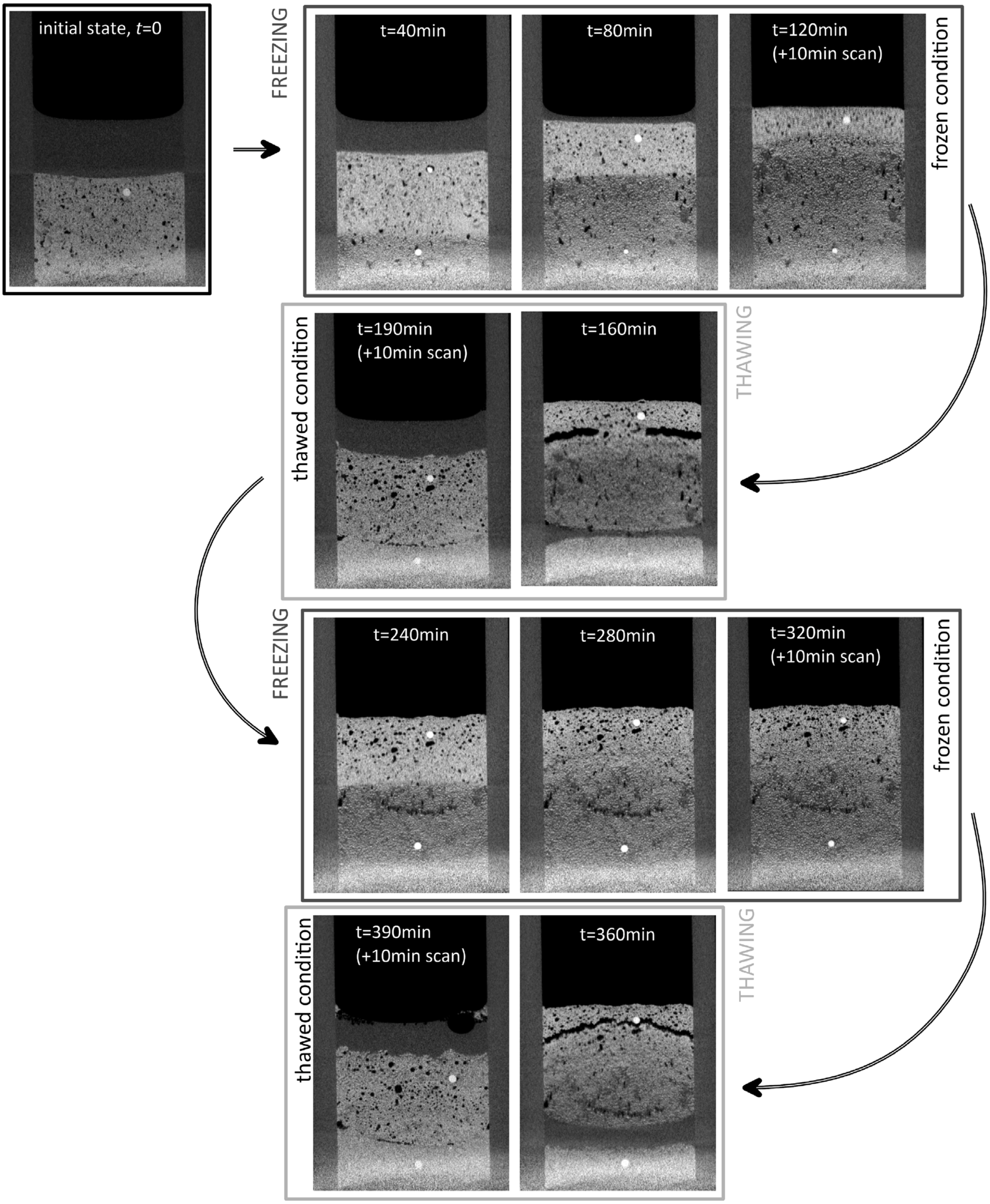

Fig. 6. Temporal sequence of images that depicts the vertical slice of the three-dimensional tomography reconstruction of the K20 sample. During freezing the temperature at the bottom of the sample is −15 °C, while during thawing it is equal to the ambient temperature T_{amb}. The top of the sample is exposed at T_{amb} for the whole test duration.

rest of the material. Segregation cracks appear as early as 30 min after thawing starts and disappear abruptly once the sample is fully thawed at $t = 190$ min, owing to the loss of adfreezing cohesion and the rehydration of the upper portion. After one freeze-thaw cycle, the sample shows residual heave and a thinner water film at the top compared to the initial state. The internal structure is significantly altered, with a residual vertical density gradient: denser at the bottom and looser at the top.

During the second freeze-thaw cycle, the liquid water is absorbed more rapidly, disappearing within 40 min from the activation the

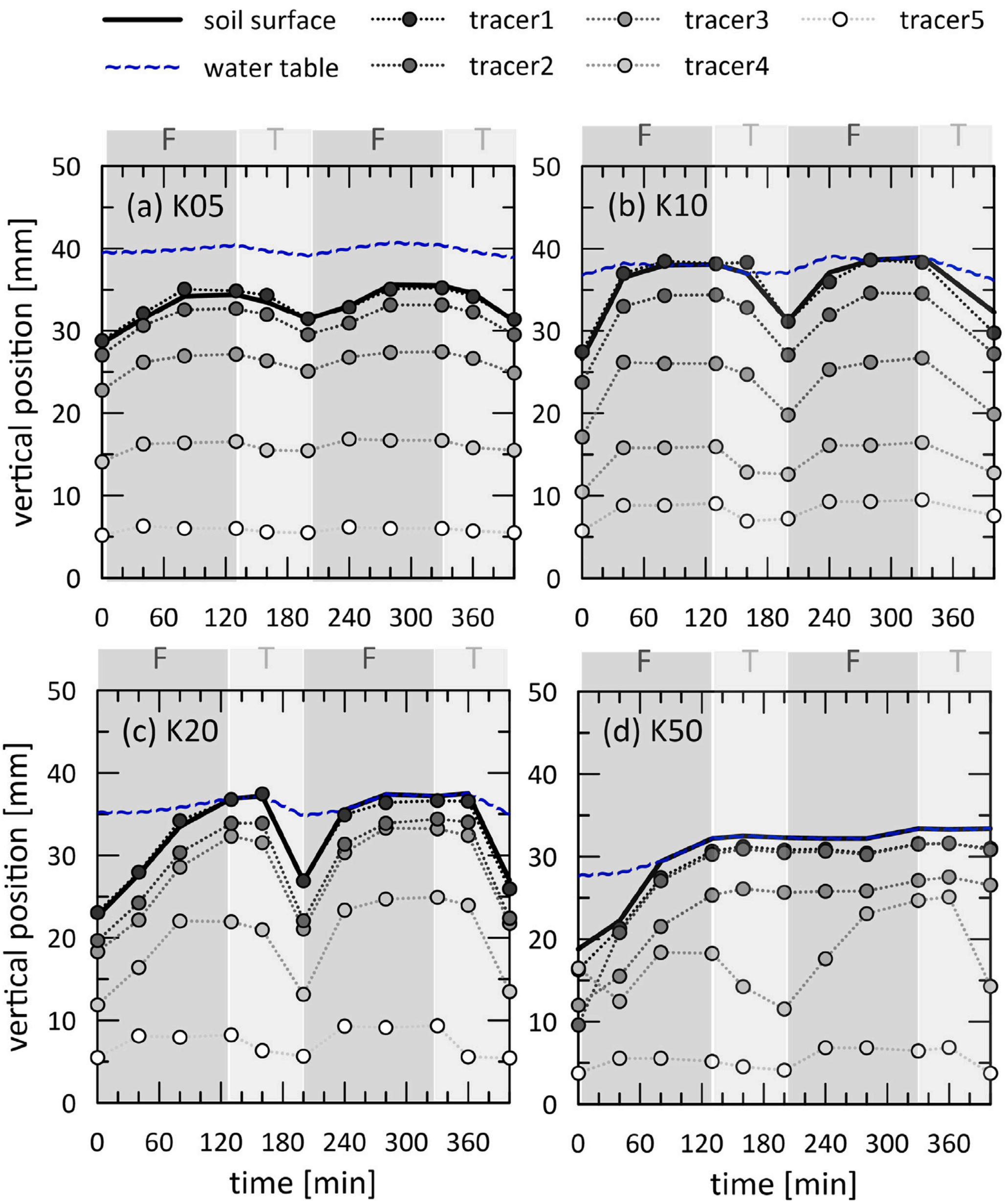

Fig. 7. Time evolution of the vertical positions of the soil surface, water level and glass bead tracers along the two freezing-thawing cycles for the four mixtures tested with clay contents of (a) K05, (b) K10, (c) K20 and (d) K50. The blue and red fields indicate the freezing (F) and thawing (T) phases, respectively.

freezing plate (t = 240 min). Furthermore, the cumulative frost heave (10.5 mm) observed during the second cycle is less pronounced than in the first.

As the fine content increases, phenomena such as frost heave, water absorption during freezing and segregation and collapses during thawing become more enhanced. A comparisons of samples with different fine contents is presented in the next section.

5. Mechanical response

5.1. Time evolution

Fig. 7 presents the time evolution of the vertical position of the soil surface, water level and glass bead tracers throughout the two freeze-thaw cycles for the four mixtures K05–K50. Heights of the soil surface and water level are estimated from one point in the central region of the sample. Surface alterations caused by boundary effects were therefore not considered. The position and the kinematic of the glass bead tracers are automatically detected through image processing.

Notably, even a small percentage of fines significantly alters both frost heave and thaw contraction, affecting the macroscopic displacements and the internal structure of the material. Increasing the clay content from 5% to 10%, as shown in Fig. 7(a–b), results in a substantial increase in the maximum cumulative heave during freezing, from approximately 7 mm in K05 to about 12 mm in K10. The position of the tracers placed at different height within the sample evolves consistently with the corresponding surface displacement, with magnitudes proportional to their distance from the base. In the K05 sample, the movements of tracers 4 and 5 are nearly negligible compared to those observed in other mixtures. Moreover, in the K10, the water film reservoir at the top is fully absorbed during freezing and subsequently released during thawing, unlike in K05, where part of the water film remains unabsorbed.

As the clay content increases further, the effects of frost heave become progressively more pronounced. While the swelling/contracting

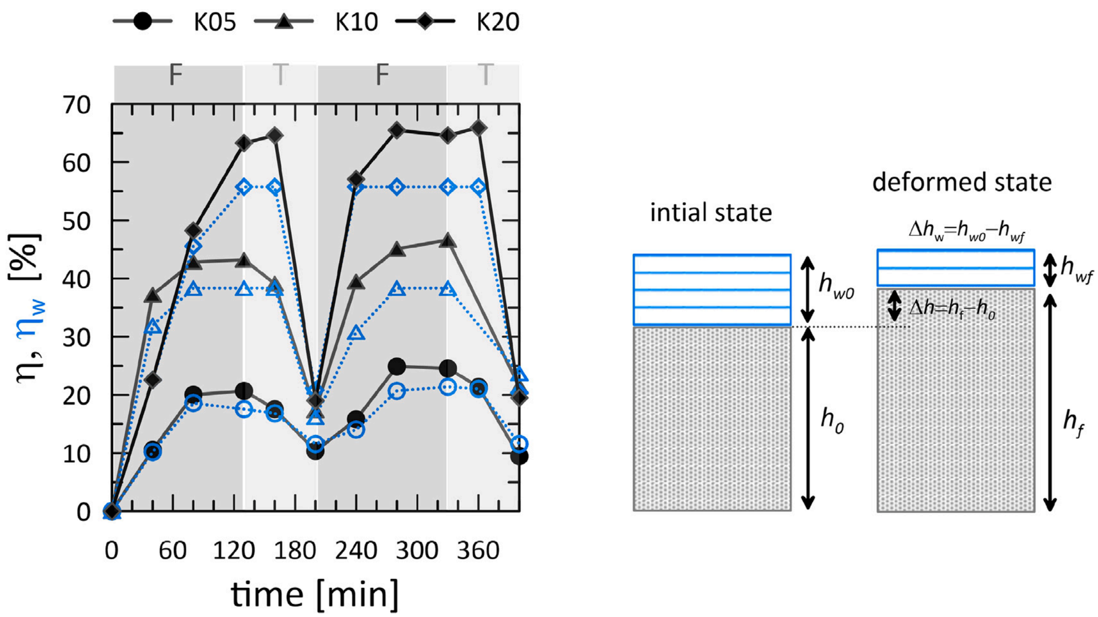

Fig. 8. Time evolution of the frost heave ratio η and water absorption ratio η_w. The dark and light grey fields indicate the freezing (F) and thawing (T) phases, respectively. The sketches on the right help identifying the quantities for estimating η and η_w.

patterns is symmetric between the two freeze-thaw cycles for mixtures K05–K10, for K20, the behaviour differs between the two cycles (Fig. 7.c). In the first cycle, the soil surface rises gradually during freezing and drops rapidly during thawing. In contrast, during the second cycle, the lifting induced by freezing occurs more rapidly than in the first.

The kinematic of K50 is by far the most complex. During the first freezing phase, the soil surface rapidly heaves by more than 10 mm, fully absorbing the water film reservoir by t = 60 min. During thawing, tracers 1–3 do not return to their original position and exhibit minimal displacement in the subsequent freeze-thaw cycle. The only tracers oscillating during freezing and thawing are tracers 4 and 5, located near the base of the sample. Their behaviour remains asymmetric despite the symmetry of the thermal loading, highlighting the non-linear response of high clay content mixtures even a lower deformation levels. Tracer 5, in particular, displays minimal vertical movement, similar to what is observed in the K05–K20 samples, still with a slight asymmetry between the two cycles.

The displacement behaviour observed in Fig. 7 is consistent with the mixture classification proposed by Park and Santamarina (2017). Coarse-dominant mixtures exhibit minimal vertical displacement, reflecting a low degree of frost susceptibility. In contrast, transitional mixtures show intermediate displacements, indicating moderate susceptibility. Finally, fine-dominant mixtures experience the highest vertical displacements and material alteration, clearly demonstrating extreme frost susceptibility.

Fig. 8 shows the evolution of frost heave ratio η and water absorption ratio η_w over time for samples K05, K10 and K20. The frost heave ratio η is a dimensionless measure of axial deformation – formally equivalent to axial strain – defined as the ratio between the change in sample height due to freezing, Δh and its initial height, h_0 (Taber, 1929):

$$\eta = \frac{\Delta h}{h_0}. \tag{3}$$

Unlike conventional strain induced by mechanical loading, this deformation arises from thermo-hydraulic processes triggered by freezing temperatures. For this reason, the term “frost heave ratio” is commonly used to emphasize its distinct physical origin. Instead, water absorption ratio η_w is defined as

$$\eta_w = \frac{\Delta h_w}{h_0}, \tag{4}$$

where Δh_w is the height of water absorbed. This parameter quantifies the axial deformation attributed specifically to water absorption. The reader can refer to the sketches in Fig. 8 to identify the heights involved in the calculation of η and η_w.

All samples exhibit an increase in frost heave ratio during freezing, followed by a decrease during thawing. The trend of η_w closely follows that of η, but remains consistently lower, indicating that most of the swelling deformation is due to water absorption. The gap $\Delta\eta$ between η and η_w can be attributed to the volume expansion of the pore water during phase change, as ice has a lower density than liquid water. Once the entire water reservoir is absorbed and freezes, the maximum value of $\Delta\eta$ can be reached. This value corresponds to approximately 9% of the combined volume fraction of the initial pore water and the water reservoir, which differs among the samples. For the samples under examination, the maximum contribution to volume expansion, due to the lower density of ice, is 6.7%, 6.9% and 8.9% for K05, K10 and K20, respectively, which approximately reflects the gaps between η and η_w in Fig. 8. A clear correlation emerges between fines content and frost heave ratio, with maximum η of 25%, 47%, 66%, for mixtures K05, K10 and K20, respectively. Mixtures with 5% and 10% fines exhibit a symmetric evolution of η throughout the test, as already shown in Fig. 7. However, as the fine content increases, asymmetry emerges in the deformation pattern. This is already visible in Fig. 7, *e.g.*, tracer 3 in K20–K50, or in the magnitude of the deformation between cycles, see tracer 1 for K20.

5.2. High clay content

The distinct mechanical response of K50 observed in Fig. 7 can only be fully understood by analysing the images taken during the test. Fig. 9 presents snapshots of the sample at different times. In the first image (a), taken at t = 40 min, the freezing front is clearly identifiable as a sharply defined, darker boundary just above tracer 1 (Fig. 9a). A vertical shrinkage crack, extending in a semicircular pattern – visible in section A2 and A3 – likely acts as a preferential path for water migration towards the freezing front. The high clay content makes the material more susceptible to solid volume reduction due to temperature drop and the development of cryogenic suction, which promotes the formation of shrinkage cracks (Taber, 1929; Chamberlain and Gow, 1979). At t = 120 min, where surface inspection confirms that the

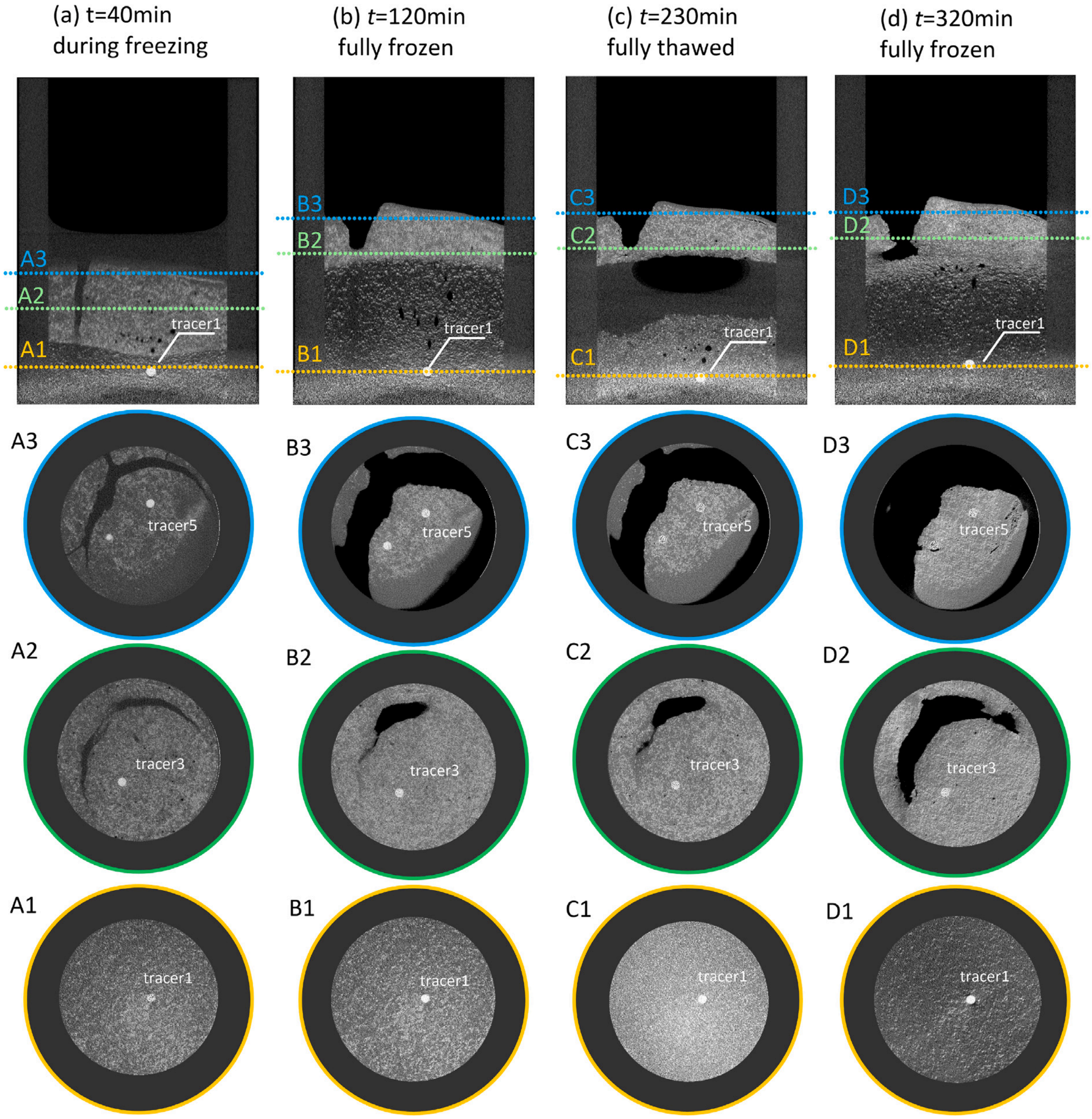

Fig. 9. Images showing the response of the soil mixture K50 along the freeze-thaw cycles. Four instants of time are documented: (a) at t = 40 min during the first freezing; (b) at t = 120 min when the sample is fully frozen; (c) at t = 220 min when the sample is fully thawed; (d) at t = 300 min when the sample is fully re-frozen. Horizontal sections correspond to the height of tracers 1,3,5.

sample is fully frozen, the crack between sections B1 and B2 disappears (Fig. 9.b). This suggests that, as freezing progresses, the material first expands to close the internal crack before continuing to heave upward. However, the presence of a wide crack at the sample surface (see Section B3) — which mirrors the shape of the one previously observed in Section A2, A3 — indicates that the original crack migrated upward into the unsaturated zone, where it further widened due to shrinkage. Notably, the upper portion of the sample in Fig. 9(b) appears denser, *i.e.*, brighter pixel colour. This area, affected by the depletion of the water reservoir, did not undergo full expansion, thereby limiting further frost heave.

Fig. 9(c) shows the sample in its fully thawed state. The position of most tracers and the soil surface does not change significantly after the first freezing cycle. The sample segregates into three distinct layers: at the bottom, a layer of thawed, saturated soil mixture; in the middle, a layer of liquid water containing a trapped air bubble; and at the top, a layer of soil mixture likely in a partially saturated state. This upper layer retains a shape similar to that observed in the frozen condition and remains suspended, likely due to friction against the sidewall of the sample. Remarkably, refreezing the sample (Fig. 9d) eliminates the segregation and restores continuity, at least in areas where sufficient water is available. The upper unsaturated portion of the sample remains elevated throughout the entire test (tracer 3, 5), whereas the lower portion undergoes vertical oscillation during freezing-thawing cycles (tracer 1). This behaviour is consistently observed in tests with high clay content. However, the exact position of shrinkage cracks, segregation patterns and resulting inhomogeneities are not repeatable due to the irreversible and non-linear nature of the process. Consequently, the interpretation of these observations remains predominantly qualitative.

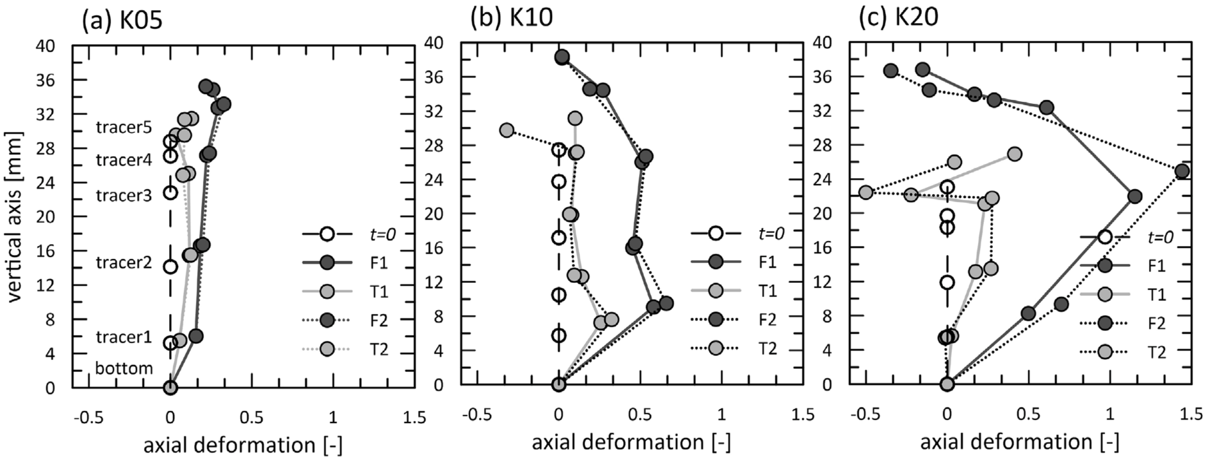

Fig. 10. Profiles of the axial strain along sample height at the end of freezing (F1, F2) and thawing (T1, T2) cycles for the samples: (a) K05; (b) K10; (c) K20. The initial position of the tracers lies on the vertical line at null strain. Positive values correspond to expansions of the soil mixture.

6. Density patterns

6.1. Local strain profiles

The kinematics of glass bead tracers are interpreted through the axial strain profile. Axial strain is estimated as the variation in distance between two consecutive tracers normalized by the initial distance. Fig. 10 presents the axial strain profiles for mixtures K05–K20 throughout the freeze-thaw cycles. For low kaolin content (K05), the axial strain profile remains relatively uniform at different stages of freezing/thawing and along the sample height. Although the deformation trends do not fully recover the initial zero-deformation state after thawing, the response is reversible after the first freezing. A similar reversible behaviour is observed for the K10 sample, although the strain distribution is less uniform along the height, with maximum expansion occurring of approximately 10 mm from the base. Additionally, after the second thawing (T2), the axial strain profile shows a sharp compaction of the top layer, indicating that the relative distance between the two top tracers (1 and 2) has decreased compared to the initial state. This is also evident in Fig. 7(b) and is likely due to an increased disturbance in the upper part of the material following two freeze-thaw cycles. In contrast, K20 exhibits a highly heterogeneous strain pattern from the first freezing path: the central region expands significantly more than the top and bottom portions of the sample. Although the strain pattern becomes more stable and somewhat reversible between subsequent freeze-thaw cycles, the initial state is not recovered. Furthermore, the top of the sample undergoes contraction during both freezing and thawing, possibly due to the development of cryogenic suction and associated water depletion.

6.2. Greylevel profiles

To examine continuous local density variations along the height of the specimen, greylevel profiles are constructed. For each horizontal slice of the 3D tomographic reconstruction, the average pixel value of a circular mask of 20 mm in diameter in the middle of the sample is calculated and then plotted against its vertical position. The size of such a mask is chosen to exclude pixels near the sidewall, in order to avoid artefacts caused by the boundary effect curvature. Higher greylevel (lighter) pixels indicate denser material, while lower greylevel (darker) pixels corresponds to less dense regions. Fig. 11 shows the greylevel profiles for tests K05, K10 and K20 at t = 0, 120, 220, 300 and 360 min. In these 16-bit images, greylevel intensities range from 0 (black) to 65 535 (white), representing 2^{16} possible shades of grey. The first 8 mm of each profile is omitted due to the white halo caused by the metal freezing plate.

For K05, the greylevel profile remains relatively uniform throughout. During freezing (F1), it decreases across the specimen, indicating a reduction in density due to volumetric expansion. A slight increase is observed during thawing (T1), although the initial state is not fully recovered. The second freeze-thaw cycle (F2-T2) closely mirrors the first, showing a stable response with no clear signs of segregation.

In K10, the first freezing phase (F1) causes a noticeable reduction in greylevel – again reflecting volume expansion – while the top region, which experiences uplift, shows a local increase. This denser zone is likely caused by water depletion combined with the development of cryogenic suction, which induces shrinkage and limits soil expansion compared to the lower layers. A similar phenomenon has been observed by Amato et al. (2022), who referred to this region as a “consolidating zone”. At t = 220 min, thawing leads to visible settlement in the upper layers and an overall increase of greylevel in the lower portion of the specimen, which had previously expanded during freezing. A segregation crack appears as a distinct local minimum in the greylevel profile. The second freeze-thaw cycle reinforces these patterns, confirming the development of heterogeneities, although the response remains reasonably consistent.

The initial profile of K20 (Fig. 11.c) shows lower greylevel compared to K05 and K10. This decreasing initial greylevel (Fig. 11 at t = 0) with increasing fine content aligns with the observation that the saturated initial void ratio tends to increase as the fine content decreases (see Table 1). The first freezing phase triggers a strong expansion up to 32 mm height and a pronounced densification at the top layer. Thawing results in significant settlement of the upper region and the persistence of segregation cracks. The second cycle (F2-T2) amplifies these effects, showing the highest degree of irreversibility and heterogeneity among the samples.

Overall, increasing fine content leads to more heterogeneous profiles, more pronounced segregation features and limited recovery of the initial structure.

7. Effect of longer freezing time

7.1. Comparison between short and tall K10 samples

No visible ice lens formed in any of the tests K05–K50 described above, likely due to the rapid freezing process and the limited height of the samples. Within two hours of lowering the freezing plate temperature to −15 °C, the material is fully frozen. According to the mechanistic theory of ice lens formation in Konrad and Morgenstern (1980), a fast-moving freezing front does not allow water to accumulate long enough to form a continuous ice lens. Instead, ice lens formation requires thermal equilibrium and a slow freezing rate.

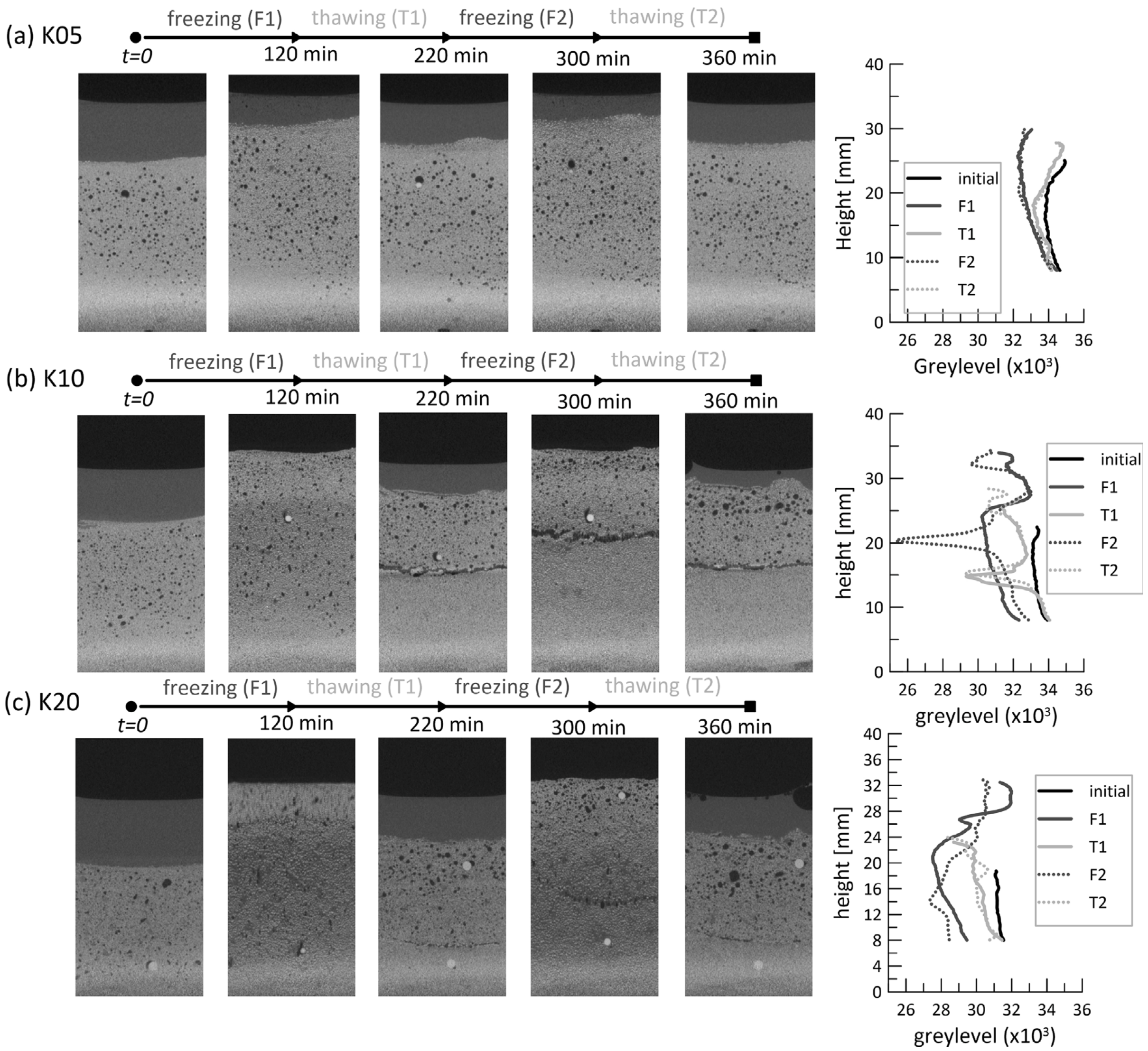

Fig. 11. Greylevel profiles of the average pixel value of a circular mask at different reference states: initial ($t = 0$), two fully frozen states ($t = 120, 300$ min) and the two fully thawed states ($t = 220, 360$ min). (a) K05, (b) K10, (c) K20. The corresponding profiles are compared in the single plot on the right.

To investigate the effect of slower freezing, an additional *in situ* X-ray tomography freeze-thaw test is conducted on a taller sample with 10% clay mixture (denoted K10_2). The initial dry and wet properties of this test are provided in Table 1. The influence of the increased sample height is assessed by comparing the time evolution of cumulative displacement for both the short sample (K10) and the tall sample (K10_2) of a same mixture, as shown in Fig. 12(a). The cumulative displacement of the tall sample (K10_2) shows a rapid initial increase, which gradually slows down and approaches a plateau after approximately five hours of freezing. During the thawing phase, no significant reduction in cumulative displacement is observed, similar to the behaviour recorded in the K50 test (see Fig. 7.d). This lack of recovery is likely due to the frictional effect of the side walls in such a tall sample, which prevents settling back during thawing. The upper portion remained uplifted, indicating material segregation, an observation further supported by the visual representations of the scans provided in the supplementary materials.

The coloured area in the figure highlights the overlapping time window (up to 130 min) in which a direct comparison between K10 and K10_2 can be made. At $t = 120$ min, the process for sample K10 is reversed to thawing, while freezing process furthers for sample K10_2. Notably, the initial displacement rates for both samples are identical, as evidenced by the overlapping curves. However, after this point, the cumulative heave of the tall sample (K10_2) becomes systematically lower than that of the short sample (K10). This difference may be attributed to the greater overburden pressure from the increased height and, more significantly, to frictional resistance along the side walls, which inhibits upward displacement.

Fig. 12(b) and (c) present vertical slice snapshots of samples K10 and K10_2 at two key times during freezing, namely: 40 min and 120 min. These slices qualitatively illustrate the position of the freezing front, identified as the boundary between the lower, looser frozen region and the upper, denser unfrozen region. In both cases, the tall sample consistently shows a lower freezing front position than the short one.

7.2. Difference images

The short time interval between acquisitions used for the K10_2 test enables difference images, where deformation phenomena are amplified and made more visible. These images are obtained by subtracting one scan from another taken at a later time, highlighting the changes between the two states. This type of image processing was not feasible for the other tests, where the time intervals between scans were too

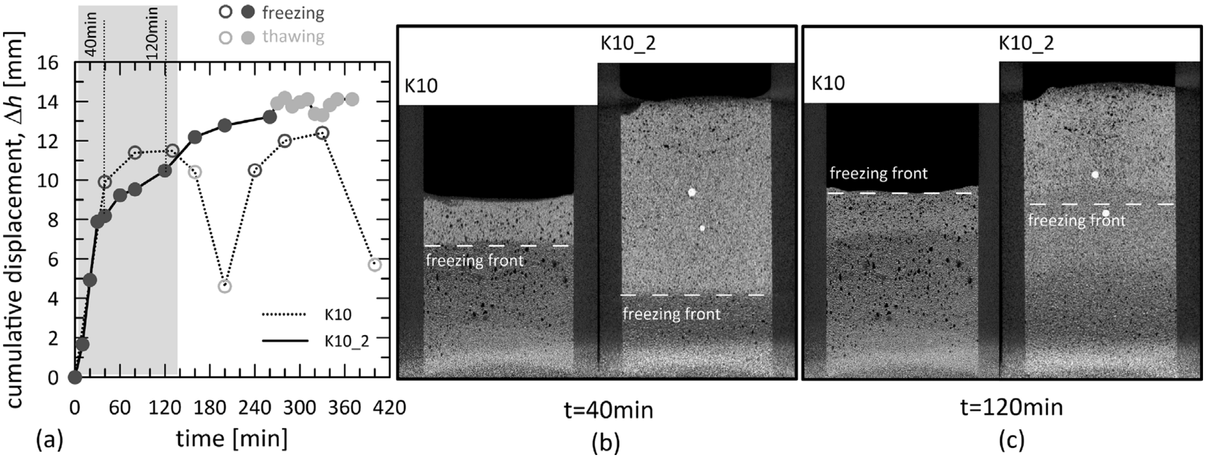

Fig. 12. Comparison between short (K10) and tall samples (K10_2) with 10% clay content. (a) Time evolution of cumulative displacement. Blue symbols represent scans taken during the freezing phase, while red symbols correspond to scans during thawing. (b) and (c) vertical slice snapshots of the two samples captured during the first freezing cycle at 40 min and 120 min, respectively.

large to detect changes that could be reliably linked to specific causes. Fig. 13 shows vertical sections of the difference images of K10_2 sample, where blue pixels indicate negative values, *i.e.*, compaction, or an increase in material density and red pixels indicate positive values, *i.e.*, expansion, or a decrease in density.

For example, comparing scans 00 (initial state) and 02 (freezing after 20 min) reveals a density increase at the top, where the material heaves during freezing and a density decrease near the base, where ice formation occurs. This decrease is especially pronounced in the early stages of freezing, as seen in the difference image 04–06. In the 06–08 difference image, the expansion zone and the freezing front become less distinct, even though the time interval between these two scans is double than in the previous ones. This is likely due to a reduced freezing rate and a depletion of the water supply at the top. An expansion zone becomes prominent again in the 08–10 difference image, where a new ice lens is about to appear. A closer inspection also reveals slight compaction (blue areas) just above the freezing front – often referred to as the “frozen fringe” – where the coexistence between ice and liquid water generates higher levels of cryogenic suction.

During thawing (second row of images in Fig. 13), a distinct blue compaction band emerges and progresses upwards from the bottom in the first three difference images (up to stage 16). Just above this band, a red extension zone appears, marking the advancing thawing front. This sequence of compression and extension bands fades around stage 16 – approximately one hour after the freezing plate is switched off – when most of the ice has presumably melted. A discontinuity forming near the top of the sample, starting from image 10–12, corresponds to a segregation crack, which gradually widens and extends downward as the lower portion consolidates during thawing. The crack stabilizes around stage 16, when deformation in the lower part ceases. Meanwhile, the top portion, which is not completely frozen, remains uplifted. This is likely due to friction with the lateral walls of the container and the presence of a partially saturated state, which enhances the cohesive strength of the soil. Additionally, the difference images highlight the displacement of the two tracers visible in all the vertical slices of Fig. 13: the red dot marks the tracer’s position in the earlier scan, while the blue dot indicates its new location, corresponding to a local increase in density.

All the qualitative observations from Fig. 13 clearly demonstrates the complex thermo-hydro-mechanical interactions that govern the behaviour of frost-susceptible soils during freeze-thaw cycles. The markedly non-linear and highly heterogeneous response explains the current difficulties of the scientific and technical community in accurately predicting frost heave and thaw-induced settlements.

8. Conclusion

It is well established in the literature that the fine content of soil critically influences its frost susceptibility. In cold regions, frost heave and thaw settlement often cause serious damage to structures and infrastructure, highlighting the need for proactive maintenance in the absence of effective mitigation strategies. This essence of problems largely stems from the lack of reliable predictive tools for the response of soils under freeze-thaw cycles. In this context, the present work investigates the impact of fine content on artificially composed clayey sand mixtures subjected to one-dimensional freeze-thaw cycles. *In situ* X-ray computed tomography, a powerful techniques to assess the material microstructural evolution, is employed to gain valuable insights into the mechanisms governing freeze-thaw behaviour.

The artificial mixtures consist of Fontainebleau sand and Speswhite kaolin in four different weight percentages, namely 5%, 10%, 20% and 50%. Additionally, two sample heights are considered for the mixture with 10% clay. The samples are initially dry-pluviated into cylindrical Perspex containers (3.0 cm internal diameter) and saturated from the bottom by immersion. Initial density of the samples increases with fine content, as even a small increase in kaolin content significantly loosens the material due to the tendency of clay particles to coat sand grains rather than settle in the inter-granular voids, creating open and unstable structures.

Freeze-thaw cycles are performed by placing the samples in contact with a cooling plate set to a temperature of −15 °C, which is switched off during thawing. The entire system, including the cooling plate, its accessories and the sample laterally insulated, is mounted on the rotation stage of an X-ray tomography chamber. 3D images of the internal structure are acquired at several deforming stages over the 6-h test, comprising two full cycles of 2 h of freezing followed by 1 h of thawing, or one cycle of a longer 4-h freezing followed by 2 h of thawing. The time-lapse tomography provides both qualitatively and quantitatively insights into the internal structural change of the material, revealing the pivotal role of fine content and the strong thermo-hydro-mechanical coupling of the process.

During freezing, samples experience significant heave, accompanied by the absorption of the water reservoir initially left at the top of the sample. The frost heave ratio shows a clear correlation with fine content, with maximum deformation during freezing ranging from 25% to 78% for mixtures containing 5% to 50% fines, respectively. The thawing phase induces an overall compaction of the samples, with the formation of segregation cracks and a diffuse degradation of the material.

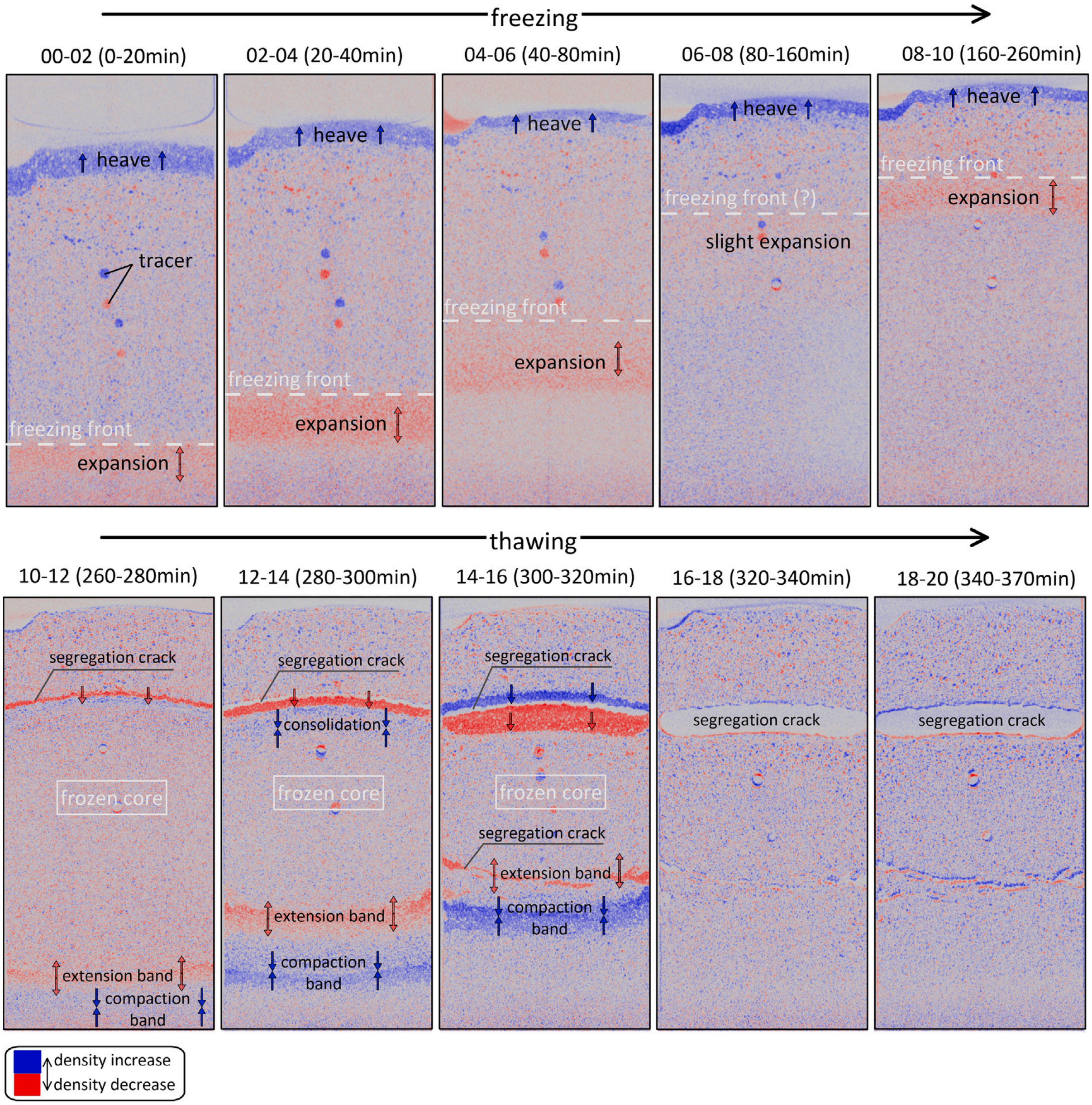

Fig. 13. Each panel shows a difference image comparing two scans taken at different times, produced by subtracting the pixel value of one scan from the other. The total number of scans in the K10_2 test is 21, denominated from 00 to 20. The difference image was performed every two scans. The first raw report difference images during freezing, while the second row during thawing.

As the fine content increases, phenomena such as frost heave, water uptake during freezing, segregation cracking during thawing and differences between successive freeze-thaw cycles become more pronounced and increasingly irreversible. While the 5% clay mixture exhibits only a nearly linear decrease in density during freezing and recovers almost entirely upon thawing, mixtures with higher fine content respond quite differently. Heterogeneous density patterns emerge particularly in mixtures with 20% and 50% clay. Their greylevel profiles show a significant decrease during freezing, indicating density reduction due to volumetric expansion. However, density remains notably higher in the uplifted regions, where depletion of the water reservoir and enhanced cryogenic suction limits further expansion. In these mixtures, most of the irreversibility is due to the first freeze-thaw cycle (see Fig. 10), after that the evolution of the profiles becomes more repeatable. Even a single freeze-thaw cycle significantly alters the internal structure: the material becomes denser near the freezing front, while the upper part remains altered and porous, resulting in a looser state compared to the initial condition. In the 50% clay mixture, deep vertical cracks develop due to cryogenic suction, leading to a strongly three-dimensional and irreversibly affected material response.

Analysis of difference image – obtained by subtracting the pixel values of a reference image from those of a deformed stage – highlights local density changes between successive stages. These appear as frost heave zones, compaction and extension bands and segregation features, underscoring the complexity of the underlying kinematics. Unfortunately, the irreversibility in the kinematic response observed in this experimental campaign is not only driven by the non-linear response in the material microstructure upon freeze-thaw cycles, but it is also quite influenced by boundary effects.

These findings contribute to a deeper understanding of freeze–thaw-induced damage in fine-containing soils and represent a step forward towards the development of more reliable predictive models and mitigation strategies for the effects induced by freeze-thaw cycles in subsurface soil of cold regions.

Future work will focus on refining the experimental setup to reduce boundary effects, to improve control of water inflow and outflow, which significantly influence the freeze-thaw response and on exploring the repeatability and conditioning effects of multiple freeze-thaw cycles. In addition, dedicated experiments are being considered to investigate the evolution of pore connectivity, which plays a key role in controlling hydraulic conductivity during and after freeze-thaw cycles. While higher-resolution imaging (*e.g.*, micro- or nano-CT) could provide more detailed insights into pore-scale processes, such resolutions are not always feasible under *in situ* conditions due to limitations in sample size and scan duration. On the modelling side, the tomographic data gathered in this study provide a solid foundation for the development and validation of numerical models capable of capturing the coupled thermo-hydro-mechanical processes during freeze-thaw cycles.

CRediT authorship contribution statement

Giulia Guida: Conceptualization, Methodology, Software, Formal analysis, investigation, Resources, Data Curation, Writing – original draft, Writing – review & editing, Visualization, Project administration, Funding acquisition. **Floriana Anselmucci:** Conceptualization, Methodology, Software, investigation, Resources, Data Curation, Writing – review & editing. **Francesca Casini:** Resources, Writing – review & editing, Supervision. **Vanessa Magnanimo:** Resources, Conceptualization, Writing – review & editing, Visualization, Supervision.

Declaration of competing interest

The authors declare the following financial interests/personal relationships which may be considered as potential competing interests: Giulia Guida reports equipment, drugs, or supplies was provided by EPOS-NL. If there are other authors, they declare that they have no known competing financial interests or personal relationships that could have appeared to influence the work reported in this paper.

Acknowledgements

The authors acknowledge EPOS-NL facilities access (https://epos-nl.nl/), enabling free-of-charge 5-day X-ray tomography scans at TU Delft.

Appendix A. Supplementary data

Supplementary material related to this article can be found online at https://doi.org/10.1016/j.coldregions.2025.104699.

Data availability

Data will be made available on request.

References

Akagawa, S., 1988. Experimental study of frozen fringe characteristics. Cold Reg. Sci. & Technol. 15 (3), 209–223.

Amato, G., Ando, E., Lyu, C., Viggiani, G., Eiksund, G.R., 2022. A glimpse into rapid freezing processes in clay with x-ray tomography. Acta Geotech. 17 (1), 327–338.

An, R., Zhang, X., Kong, L., Gong, J., Lei, X., 2021. Artificial ground freezing impact on shear strength and microstructure of granite residual soil under an extremely low temperature. Front. Earth Sci. 9, 772459.

Arenson, L.U., Sego, D.C., Take, W.A., 2007. Measurement of ice lens growth and soil consolidation during frost penetration using particle image velocimetry (PIV). In: 60th Canadian Geotechnical Conference, Ottawa, ON. pp. 2046–2053.

Armstrong, M.D., Csathy, T.I., 1963. Frost design practice in canada-and discussion. Highw. Res. Rec. (33).

Calmels, F., Allard, M., 2008. Segregated ice structures in various heaved permafrost landforms through CT scan. Earth Surf. Process. Landforms: J. British Geomorphol. Res. Group 33 (2), 209–225.

Casagrande, A., 1931. Discussion of frost heaving. In: Proceedings, Highway Research Board. vol. 11, pp. 168–172, Pt 1.

Chamberlain, E.J., 1982. Frost susceptibility of soil–review of index tests.

Chamberlain, E.J., Gow, A.J., 1979. Effect of freezing and thawing on the permeability and structure of soils. In: Developments in Geotechnical Engineering. vol. 26, Elsevier, pp. 73–92.

Cubrinovski, M., Ishihara, K., 2002. Maximum and minimum void ratio characteristics of sands. Soils Found. 42 (6), 65–78.

Cui, L., Chen, J., Xiao, Z., Yuan, Q., Zhao, X., Xue, J., 2024. A simple model of the soil freezing characteristic curve for saline soils with two freezing stages. J. Hydrol. 637, 131378.

Dalla Santa, G., Cola, S., Secco, M., Tateo, F., Sassi, R., Galgaro, A., 2019. Multiscale analysis of freeze–thaw effects induced by ground heat exchangers on permeability of silty clays. Geotechnique 69 (2), 95–105.

Defrise, M., 2001. A short reader's guide to 3D tomographic reconstruction. Comput. Med. Imaging Graph. 25 (2), 113–116.

Fan, W., Yang, P., Yang, Z.J., 2021. Freeze-thaw impact on macropore structure of clay by 3D X-ray computed tomography. Eng. Geol. 280, 105921.

Haosong, H., Teng, J., Zhao, S., Guan, W., Zhang, S., 2024. Comparative evaluation of the methods of assessing frost heave susceptibility. Cold Reg. Sci. & Technol. 104406.

Hjort, J., Streletskiy, D., Doré, G., Wu, Q., Bjella, K., Luoto, M., 2022. Impacts of permafrost degradation on infrastructure. Nat. Rev. Earth Environ. 3 (1), 24–38.

Hohmann-Porebska, M., 2002. Microfabric effects in frozen clays in relation to geotechnical parameters. Appl. Clay Sci. 21 (1–2), 77–87.

Kalvoda, L., Kichanov, S.E., Kučeráková, M., Lukin, E.V., Vratislav, S., 2019. Ice melting kinetics in sand–water mixtures investigated by neutron radiography and diffraction. J. Cold Reg. Eng. 33 (3), 04019003.

Konrad, J.-M., 1999. Frost susceptibility related to soil index properties. Can. Geotech. J. 36 (3), 403–417.

Konrad, J.-M., Morgenstern, N.R., 1980. A mechanistic theory of ice lens formation in fine-grained soils. Can. Geotech. J. 17 (4), 473–486.

Martinez-Garcia, J., Gwerder, D., Wahli, F., Guarda, D., Fenk, B., Stamatiou, A., Worlitschek, J., Schuetz, P., 2023. Volumetric quantification of melting and solidification of phase change materials by in-situ X-ray computed tomography. J. Energy Storage 61, 106726.

Mitchell, J.K., Soga, K., et al., 2005. Fundamentals of Soil Behavior, vol. 3, John Wiley & Sons New York.

Nakamura, D., Song, B., Kawaguchi, T., Kawajiri, S., 2021. Development of a technique for observing the frost heaving process in soil using an industrial micro-focus X-ray CT scanner. Geomate J. 21 (84), 112–120.

Nishimura, S., Gens, A., Olivella, S., Jardine, R., 2009. THM-coupled finite element analysis of frozen soil: formulation and application. Géotechnique 59 (3), 159–171.

Othman, B.A., Marto, A., 2018. Laboratory test on maximum and minimum void ratio of tropical sand matrix soils. In: IOP Conference Series: Earth and Environmental Science. vol. 140, IOP Publishing, 012084, 1.

Park, J., Santamarina, J.C., 2017. Revised soil classification system for coarse-fine mixtures. J. Geotech. Geoenvironmental Eng. 143 (8), 04017039.

Peppin, S.S., Style, R.W., 2013. The physics of frost heave and ice-lens growth. Vadose Zone J. 12 (1), 1–12.

Purwana, Y.M., Nikraz, H., 2015. The characteristic of sand-kaolin clay mixture as artificial material for laboratory soil testing. In: Geotechnique, Construction Materialss & Environment. vol. 5, GEOMATE.

Taber, S., 1929. Frost heaving. J. Geol. 37 (5), 428–461.

Thevanayagam, S., Fiorillo, M., Liang, J., 2000. Effect of non-plastic fines on undrained cyclic strength of silty sands. In: Soil Dynamics and Liquefaction 2000. pp. 77–91.

Tian, H., Wei, C., Lai, Y., Chen, P., 2018. Quantification of water content during freeze–thaw cycles: A nuclear magnetic resonance based method. Vadose Zone J. 17 (1), 1–12.

Torrance, J., Elliot, T., Martin, R., Heck, R., 2008. X-ray computed tomography of frozen soil. Cold Reg. Sci. & Technol. 53 (1), 75–82.

Viggiani, G., Andò, E., Takano, D., Santamarina, J., 2015. Laboratory X-ray tomography: a valuable experimental tool for revealing processes in soils. Geotech. Test. J. 38 (1), 61–71.

Viglianti, A., Guida, G., Casini, F., 2024. Freezing-thawing response of sand-kaolin mixtures in oedometric conditions. In: E3S Web of Conferences. vol. 544, EDP Sciences.

Vu, Q.H., Pereira, J.-M., Tang, A.M., 2022. Effect of fines content on soil freezing characteristic curve of sandy soils. Acta Geotech. 17 (11), 4921–4933.

Zhou, J., Pei, W., Zhang, X., Liu, W., Wei, C., 2022. An easy method for assessing frost susceptibility of soils: the freezing ring test. Acta Geotech. 17 (12), 5691–5707.